



Nonlinear water wave interaction with floating bodies in SPH



B. Bouscasse ^{a,b}, A. Colagrossi ^{a,*}, S. Marrone ^a, M. Antuono ^a

^a CNR-INSEAN, The Italian Ship Model Basin, Rome, Italy

^b Aeronautics Department (ETSIA), Technical University of Madrid (UPM), 28040 Madrid, Spain

ARTICLE INFO

Article history:

Received 7 August 2012

Accepted 13 May 2013

Available online 4 July 2013

Keywords:

Smoothed particle hydrodynamics

Free-surface flows

Fluid body interaction

Ghost-fluid method

Numerical water tank

Floating body

ABSTRACT

A weakly compressible SPH solver is presented for applications involving nonlinear interaction between water waves and floating bodies. A complete algorithm able to compute fully coupled viscous Fluid–Solid interactions is described. No slip boundary condition on the solid surface is enforced through a ghost–fluid technique and the global loads are evaluated through the momentum exchange between fluid and ghost particles. A dedicated algorithm is developed to manage the intersection between the free surface and the solid profile. An explicit synchronous algorithm is proposed for the full coupling between fluid and rigid bodies. Stability, convergence and conservation properties are tested on several freely floating test cases and a final validation of the full algorithm is performed for the interaction between a 2-D box and a wave packet.

© 2013 Elsevier Ltd. All rights reserved.

1. Introduction

Violent interaction between waves and floating bodies is a topic of large interest in the naval, coastal and ocean engineering fields. Indeed, oil vessels and platforms for exploration and production, barges, pontoons, energy devices, fish farms are just some examples of engineering projects in need of studies about such a problem. The present paper is dedicated to the simulation of strong non-linear interactions between a fluid and floating bodies through a Smoothed Particle Hydrodynamics model.

Historically, the modelling of Numerical Wave Tanks (NWTs) for the interaction between fluid and rigid bodies has been developed in the framework of potential flow theory by using the Mixed Eulerian-Lagrangian Boundary Element Method (BEM-MEL) introduced by Longuet-Higgins and Cokelet (1976) and followed by Faltinsen (1977) and Vinje and Brevig (1981). Nonlinear potential flow solvers allow long-time simulations at a moderate computational time and, consequently, are very useful for engineering applications related to safety of ships and offshore platforms in severe sea-state conditions (see e.g. Ferrant, 1998; Greco, 2001). The main drawback of these numerical models is the low robustness and the inability to describe viscous flows, wave breaking and fragmentation of the air–water surface.

The need to go beyond such limitations encouraged the development of mesh-based Navier–Stokes models for solving free-surface flows. The most popular techniques used to treat the free surface are the Level Set (LS) function, the Volume Of Fluid (VOF) and the Constrained Interpolation Profile (CIP) (see respectively e.g. Hirt and Nichols, 1981; Sethian, 1999; Yabe et al., 2001). Besides this, the simulation of a fully non-linear interaction between waves and floating bodies presents a number of difficult numerical issues, and is still considered a challenging problem. The full coupling between the fluid and rigid body requires some specific considerations. The floating body dynamics involve a relatively large time scale and act

* Corresponding author. Tel.: +39 06 50 299 343; fax: +39 06 50 70 619.

E-mail addresses: benjamin.bouscasse@cnr.it (B. Bouscasse), andrea.colagrossi@cnr.it (A. Colagrossi), salvatore.marrone@cnr.it (S. Marrone), matteo.antuono@cnr.it (M. Antuono).

around the equilibrium state, that is a very critical condition for the stability of any fluid solid interaction (FSI) code. Other difficulties are related to the motion of floating bodies inside the fluid domain. This is generally modelled by using sliding/deforming meshes (see e.g. Hǎdžić et al., 2005), dynamic overlapping grids (see e.g. Broglia et al., 2009; Di Mascio et al., 2008) or by representing the body through an immersed boundary technique (first defined in Peskin, 1977 and further developed in Hu and Kashiwagi, 2009; Yang and Stern, 2012).

More recently, particle methods, such as the Smoothed Particle Hydrodynamics (SPH) or the Moving Particles Semi-implicit (MPS) methods, have shown promising results in this context. In particular, in the present work we use the δ -SPH variant defined in Antuono et al. (2010) and validated for NWT application in Antuono et al. (2011). In principle, the meshless character of the SPH/MPS methods permits to treat the free motions of a body inside the fluid domain in a easier way respect to mesh-based solvers. Koshizuka et al. (1998) were the first to simulate a small body interacting with a breaking wave using the MPS particle method (see also Naito and Sueyoshi, 2002). Concerning the SPH method, the first simulation of a solid body interacting with fluid was done by Monaghan and Kos (2000). Fluid body coupling with SPH was also performed in May and Monaghan (2003), Monaghan et al. (2003), Shao and Gotoh (2004), Oger et al. (2006), Delorme et al. (2006) and Omidvar et al. (2012). In Oger et al. (2006), an extensive validation has been performed on a test involving the water entry of a wedge. Recently, in Ulrich and Rung (2012) the case of a water entry of a cube is discussed and the numerical evolution is qualitatively validated through comparison with snapshots from experiments while in Omidvar et al. (2013) a 3D variable mass particle model is proposed for studying floating bodies. In Kajtar and Monaghan (2008) and Hashemi et al. (2012) descriptions of algorithms for the coupling between fluid and rigid bodies are proposed. Recently the SPH method has been used also in the more general issue of the violent fluid–solid interaction (see e.g. Eghtesad et al., 2012; Marsh et al., 2010).

Beside this, the highly nonlinear interaction between gravity waves and floating bodies for NWT applications has still not been sufficiently addressed in the particle method literature.

The present paper is a first attempt to solve complex viscous flows involving floating bodies. Even in a 2-D framework a large number of particles is necessary to correctly describe viscous phenomena and the large time scales involved. In this context the main drawback of the SPH method is that it is not straightforward to use multi-spatial resolution models. However, different attempts to overcome this issue are present in the recent literature (see e.g. Hashemi et al., 2012; Ulrich and Rung, 2012) and, therefore, improvements on this topic are left for future researches.

In the present work an extensive study of the interaction between fluid and floating bodies is proposed, providing accurate formulae for the evaluation of forces and torques and comparisons with experiments available in the literature. The correct simulation of this kind of problems requires an accurate development of some specific features of the SPH. A crucial point is the attainment of the correct stable equilibrium for a floating body which is not subjected to excitation. With respect to this, the definition of accurate formulae is of fundamental importance for the evaluation of the forces and torques on the body. In the present work, the theoretical derivation of these expressions and check that the momenta and energy exchanges between fluid and moving bodies is shown to be correctly modelled. A further fundamental aspect for a sound and reliable numerical description of floating bodies is the modeling of the intersection between body and the free surface. This point has been addressed in details in Section 3.1.

The paper is organized as follows: Section 2 briefly presents the δ -SPH equations while in Section 3 a ghost–fluid technique is described to enforce the no-slip boundary condition on complex solid geometries. Using the ghost–fluid approach, complete formulae for the evaluation of forces and torques on bodies are obtained (Section 3.2) while the coupling algorithm is discussed in Section 4. Finally, in Section 5 different test cases of increasing complexity are proposed. Those cases demonstrate that the proposed model is able to handle challenging fluid body interactions and to achieve accurate results when comparing the numerical output data to reference solutions.

2. δ -SPH equations

In the present work the δ -SPH scheme proposed by Antuono et al. (2010) is adopted. The fluid is assumed to be barotropic and weakly compressible and the reference equations are the Navier–Stokes equations. A simple linear state equation, namely $p = c_0^2(\rho - \rho_0)$, is used to match the pressure and density field. Here, c_0 is the sound speed and ρ_0 is the density along the free surface for a fluid at rest. The speed of sound c_0 is set in order to guarantee density variation smaller than $0.01\rho_0$.

The δ -SPH scheme reads

$$\left\{ \begin{array}{l} \frac{D\rho_i}{Dt} = -\rho_i \sum_j (\mathbf{u}_j - \mathbf{u}_i) \cdot \nabla_i W_{ij} V_j + \delta h c_0 \sum_j \psi_{ij} \frac{(\mathbf{r}_j - \mathbf{r}_i) \cdot \nabla_i W_{ij}}{\|\mathbf{r}_j - \mathbf{r}_i\|^2} V_j, \\ \frac{D\mathbf{u}_i}{Dt} = -\frac{1}{\rho_i} \sum_j (p_j + p_i) \nabla_i W_{ij} V_j + \mathbf{f}_i + \nu \frac{\rho_0}{\rho_i} \sum_j \pi_{ij} \nabla_i W_{ij} V_j, \\ \frac{De_i}{Dt} = -\frac{p_i}{\rho_i} \sum_j (\mathbf{u}_j - \mathbf{u}_i) \cdot \nabla_i W_{ij} V_j + \nu \frac{\rho_0}{\rho_i} \sum_j \pi_{ij} (\mathbf{u}_j - \mathbf{u}_i) \cdot \nabla_i W_{ij} V_j, \\ \frac{D\mathbf{r}_i}{Dt} = \mathbf{u}_i, \end{array} \right. \quad (1)$$

where ρ_i , p_i , \mathbf{u}_i , V_i and e_i are respectively the density, the pressure, the velocity, the volume and the internal energy of the i -th particle. Symbols ν and \mathbf{f}_i indicates respectively the kinematic viscosity and the body force acting on the i -th particle, while ∇_i denotes the differentiation with respect to the position of the i -th particle. Finally, W_{ij} is the kernel function. In this work a Renormalized Gaussian kernel (see e.g. Molteni and Colagrossi, 2009) has been used. W has a compact support of radius $3h$, where h is the *smoothing length*. For $h \rightarrow 0$ the system (1) converges to the Navier–Stokes equations (see e.g. Colagrossi et al., 2011).

The main feature of the δ -SPH scheme relies on the use of an artificial diffusive term into the continuity equation in order to remove the spurious numerical high-frequency oscillations in the pressure field. The arguments of the diffusive and viscous terms are respectively

$$\psi_{ij} = 2(\rho_j - \rho_i) - (\langle \nabla \rho \rangle_i^L + \langle \nabla \rho \rangle_j^L) \cdot (\mathbf{r}_j - \mathbf{r}_i),$$

$$\pi_{ij} = K \frac{(\mathbf{u}_j - \mathbf{u}_i) \cdot (\mathbf{r}_j - \mathbf{r}_i)}{\|\mathbf{r}_j - \mathbf{r}_i\|^2},$$

where $K = 2(n+2)$ and n is the spatial dimension of the problem at hand. Symbol $\langle \nabla \rho \rangle_i^L$ indicate the renormalized density gradient (see Randles and Libersky, 1996 for more details). The (dimensionless) parameter δ is set equal to 0.1 in all the simulations.

The viscous forces are modelled through the viscous formula of Monaghan and Gingold (1983) that preserves both linear and angular momenta.

As concerns the stability criteria for the viscous SPH scheme, we found heuristically that the pressure field remains stable when the local Reynolds number defined with the smoothing length, $Re_h = Uh/\nu$, is not larger than $\mathcal{O}(10)$ (see also Marrone, 2012). For all the test cases presented in the manuscript $Re_h \sim \mathcal{O}(1) - \mathcal{O}(10)$. The values chosen for Re_h are also small enough to ensure the resolution of the boundary layer on the solid surfaces.

In system (1) the energy equation is uncoupled with the momentum one and it is just used to check the conservation of the total energy of the particles system. Indeed, in the absence of solid walls and external forces system (1) conserves the total energy exactly (see e.g. Benz, 1989). Generally, this is no longer true in the presence of solid walls because of the numerical enforcement of the boundary conditions. Then, a check on the energy conservation is made *a posteriori* (see Section 5).

The fluid particles are initially positioned using the algorithm described in Colagrossi et al. (2012). Thanks to this procedure, at the initial instant all particles have approximately the same volume, namely V_0 , which is equal to the fluid domain volume divided by the number of fluid particles. Consistently, the particle mean spacing is denoted by $\Delta x = V_0^{1/n}$. The average number of particles in the kernel support is set by choosing the ratio $h/\Delta x$. In the present work $h/\Delta x$ is set equal to 1.33 which in two dimensions corresponds to about 50 interacting particles.

Along with the volume distribution, the initial pressure and the velocity fields are prescribed as well. The initial density distribution $\rho_i(t_0)$ is evaluated by means of the state equation and the particle masses are computed through the equation $m_i = V_0 \rho_i(t_0)$. The mass of the i -th particle remains constant during the time evolution ensuring the total mass conservation of the particles system. The volume distribution is updated in time using the density field, i.e. $V_i(t) = m_i/\rho_i(t)$.

3. Enforcement of the solid-boundary condition through a ghost–fluid method

In the present work the ghost–fluid technique is used to enforce the boundary conditions on the body surface. Specifically, the solid domain is modelled through a set of “imaginary particles” (hereinafter denoted as “ghost particles” and labelled with the subscript “s”) and all the fluid fields (that is, velocity, pressure and internal energy) are extended on these fictitious particles through appropriate mirroring techniques. Different mirroring techniques are adopted to enforce different boundary conditions (e.g., Dirichlet or Neumann conditions). To this end, the solid surface is discretized in equispaced body nodes and a layer of ghost particles is disposed in the solid region. The ghost particle positions have been obtained by using the technique described in Marrone et al. (2011a) and in Marrone et al. (2011b) (see the sketch in the left plot of Fig. 1). The pressure, velocity and internal energy assigned to the fixed ghost particles, namely (\mathbf{u}_s, p_s, e_s) , are computed by using the values obtained at specific interpolation nodes internal to the fluid and uniquely associated with the fixed ghost particles. Hereinafter, the interpolated values are indicated through (\mathbf{u}^*, p^*, e^*) .

The internal energy is mirrored on the fixed ghost particles to enforce the Neumann condition $\partial e / \partial \mathbf{n} = 0$, where \mathbf{n} is the normal unit vector to the solid profile. This means that no heat flux is allowed across the solid boundary. Similarly, the pressure field p_s is mirrored on the fixed ghost particles to enforce the following Neumann condition:

$$\frac{\partial p}{\partial \mathbf{n}} = \rho \left[\mathbf{f} \cdot \mathbf{n} - \frac{D\mathbf{u}_b}{Dt} \cdot \mathbf{n} + \mu \nabla^2 \mathbf{u} \cdot \mathbf{n} \right], \quad (2)$$

where \mathbf{f} is a generic body force and \mathbf{u}_b is the velocity of the solid boundary (for details see Marrone et al., 2011a). The last term can be neglected for the Reynolds numbers adopted in this work. This leads to

$$p_s = p^* + \frac{\partial p}{\partial \mathbf{n}} \cdot (\mathbf{r}^* - \mathbf{r}_s). \quad (3)$$

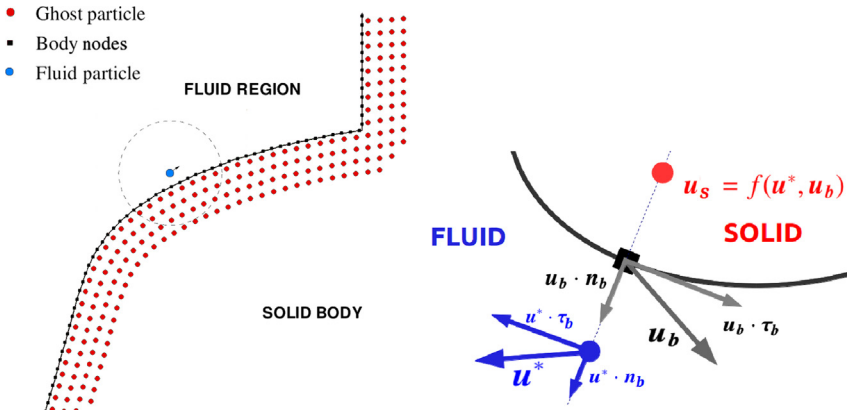


Fig. 1. Sketch of the ghost–fluid approach. Left: Discretization of the ghost–fluid through ghost particles. Right: Mirroring of the velocity.

The velocity field is object of a specific treatment. As sketched in the right plot of Fig. 1, the ghost velocity \mathbf{u}_s depends on both \mathbf{u}^* and \mathbf{u}_b , the latter being the velocity of the nearest body node. De Leffe et al. (2011) found that different mirroring techniques have to be used to evaluate $\langle \nabla \cdot \mathbf{u} \rangle$ and $\langle \nabla^2 \mathbf{u} \rangle$ and to avoid inconsistencies and loss of accuracy. The specific mirroring techniques treat differently the components of \mathbf{u}^* in the normal and tangential direction to the solid surface (right plot of Fig. 1).

De Leffe et al. (2011) proved that the velocity-divergence operator is convergent and consistent if the normal component of \mathbf{u}^* is mirrored in the frame of reference of the solid profile (see Colagrossi and Landrini, 2003), leaving the tangential component unaltered

$$\langle \nabla \cdot \mathbf{u} \rangle_i = \sum_j (\mathbf{u}_j - \mathbf{u}_i) \cdot \nabla_i W_{ij} V_j \quad \begin{cases} \mathbf{u}_s \cdot \mathbf{n} = 2\mathbf{u}_b \cdot \mathbf{n} - \mathbf{u}^* \cdot \mathbf{n} \\ \mathbf{u}_s \cdot \mathbf{\tau} = \mathbf{u}^* \cdot \mathbf{\tau}. \end{cases} \quad (4)$$

Conversely, to evaluate the divergence of the viscous stress $\langle \nabla \cdot \mathbb{V} \rangle$, the velocity field has to be mirrored to approximate no-slip conditions along the solid bodies. A common way (adopted in this work) is to reverse the tangential component, leaving the normal one unaltered

$$\langle \nabla \cdot \mathbb{V} \rangle = \rho_0 \nu \sum_j \pi_{ij} \nabla_i W_{ij} V_j \quad \begin{cases} \mathbf{u}_s \cdot \mathbf{n} = \mathbf{u}^* \cdot \mathbf{n} \\ \mathbf{u}_s \cdot \mathbf{\tau} = 2\mathbf{u}_b \cdot \mathbf{\tau} - \mathbf{u}^* \cdot \mathbf{\tau}. \end{cases} \quad (5)$$

Indeed, similarly to the procedure adopted for the velocity divergence where the velocity tangential component is left unaltered in the ghost fluid region, in Eq. (5) the velocity normal component is not mirrored to not introduce numerical errors in the evaluation of $\langle \nabla \cdot \mathbb{V} \rangle$.

3.1. Numerical treatment of the intersection between the free surface and the body

In order to correctly treat the intersection between the free surface and solid boundaries, it is necessary to implement an algorithm able to determine when a portion of the ghost–fluid region is immersed or not. To this purpose, the condition immersed/not immersed of a ghost particle is defined by the state of the associated interpolation node. We consider now the sketch in left plot of Fig. 2 where an interpolation node is positioned outside the fluid domain at distance d from the free surface. The position of the interpolation node with respect to the free surface is evaluated through a Level-Set function ϕ that represents the signed distance of the interpolation node from the free surface, namely $d = |\phi|$. When $\phi \leq 0$, the node is immersed in the fluid domain and the physical quantities on the ghost particle are obtained by using Eqs. (2), (4), and (5). When $\phi > 0$, the interpolation node is out of the fluid domain and it is necessary to switch off the interpolation node and the associated ghost particle.

In the case $\phi > 3h$, the distance of the interpolation node from the free surface is greater than the (adopted) kernel support and, consequently, all the interpolated values are naturally zero since there are no neighbour fluid particles. In the case $0 < \phi < 3h$, part of the kernel support is covered by the fluid domain and non-physical values of p, \mathbf{u} and e are interpolated on the node. To identify the nodes falling within the latter case, the function $\xi(\mathbf{r})$ is introduced

$$\xi(\mathbf{r}) = \frac{h}{2} \frac{|\sum_i \nabla W(\mathbf{r} - \mathbf{r}_i) V_i|}{\sum_j W_j(\mathbf{r} - \mathbf{r}_j) V_j}. \quad (6)$$

This function is evaluated at the node position and its value is used to decide when an interpolation node has to be switched off. When the node is inside the fluid and $\phi \leq -3h$, $\xi(\mathbf{r})$ is close to zero, since in Eq. (6) the numerator is approximately null and the denominator is close to 1.

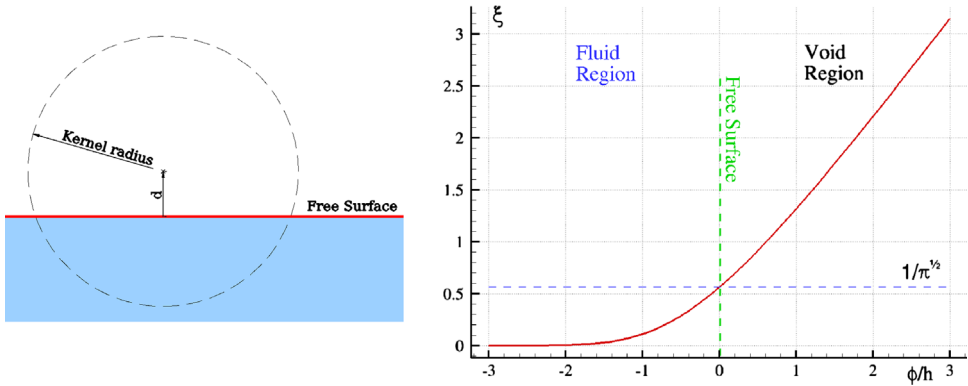


Fig. 2. Sketch of the procedure to identify nodes inside/outside the fluid domain. Left: sketch of an interpolation node outside the fluid domain at distance d from the free surface. Right: behaviour of the function ξ (see Eq. (6)) by varying ϕ .

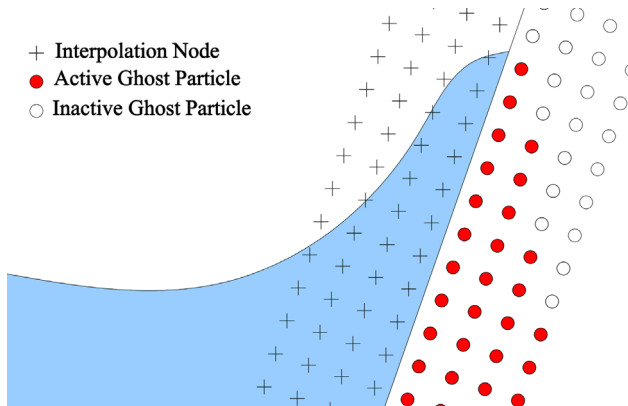


Fig. 3. Sketch of the activated ghost particles at the intersection between the free surface and the body surface.

Now, let us consider the case of a node on the free surface, *i.e.* $d=0$. If the free surface is regular and h is small enough, the free surface in the neighbourhood of the node can be approximated with a straight line and the function $\xi(\mathbf{r})$ is almost equal to $1/\sqrt{\pi}$ (using a renormalized Gaussian kernel). Note that, in the neighbourhood of the free surface, $\xi(\mathbf{r})$ increases almost linearly with ϕ (see the right plot of Fig. 2). Then, the simplest choice would be to switch off the nodes where $\xi(\mathbf{r}) \geq 1/\sqrt{\pi}$. Unfortunately, the free surface is generally not very regular and cannot be approximated through a straight line. Then, a conservative threshold for ξ has been chosen. Specifically, a node at the position \mathbf{r}_N for which $\xi(\mathbf{r}_N) = 0.8$ is still considered inside the fluid. This threshold is kernel dependent, and the value 0.8 is here obtained using a Renormalized Gaussian kernel.

Fig. 3 displays a sketch of the whole procedure described above. The ghost particles that have the corresponding interpolation node inside the fluid domain are active (coloured in red in the sketch) and their physical quantities are obtained according to Eqs. (2), (4), and (5). The ghost particles associated to nodes which are outside the fluid domain are inactive, that is, they are not visible by the fluid particles.

Even if the method proposed for switching on and off the ghost particles is a binary method, no instabilities or genesis of spurious acoustic signals have been observed. This technique has been used also for solving strong water impacts (see Marrone et al., 2011a) and, even for such flows (characterized by high pressure gradients) no instabilities due to the proposed algorithm have been observed.

3.2. Evaluation of forces and torques using the ghost–fluid technique

To find out the formulation for global loads exerted by the fluid on solid structures, it is convenient to develop the analysis at the continuum level. The fluid and solid domains are denoted by Ω_f and Ω_s respectively. The forces on solid bodies can be evaluated by using two main approaches: the evaluation of the forces integrating the stresses along the body surface and the technique here proposed where, similarly to Doring (2005), a volume integral over the ghost particle domain is used. In the following, the equivalence of these two approaches is given (mathematical details have been reported in Appendix A).

Denoting by $\langle \mathbb{T} \rangle$ the smoothed stress tensor, the global force on the body is

$$\mathcal{F}_{\text{fluid-solid}} = \int_{\partial\Omega_s} \langle \mathbb{T} \rangle \cdot \mathbf{n} dS, \quad (7)$$

where \mathbf{n} is the unit outward normal to the solid profile. Assuming the flow field to be mirrored on the solid body through a ghost-fluid technique, the stress tensor can be decomposed in

$$\langle \mathbb{T} \rangle(\mathbf{r}) = \int_{\Omega_f} \mathbb{T}' W(\mathbf{r}' - \mathbf{r}) dV' + \int_{\Omega_s} \mathbb{T}^* W(\mathbf{r}^* - \mathbf{r}) dV^*, \quad (8)$$

where the starred variables indicate quantities mirrored over the solid domain Ω_s . Substituting (8) into (7) and using the divergence theorem and the symmetry properties of the kernel function, we obtain the following equality:

$$\mathcal{F}_{\text{fluid-solid}} = \int_{\Omega_f} dV \int_{\Omega_s} (\mathbb{T}^* + \mathbb{T}) \cdot \nabla W(\mathbf{r}^* - \mathbf{r}) dV^* + \mathcal{O}(h), \quad (9)$$

where ∇ indicates the differentiation with respect to the position \mathbf{r} . The terms of order $\mathcal{O}(h)$ indicate the contributions due to the presence of the free surface. These terms are small since, by definition, the tension along the free surface is zero.

When Eq. (9) is discretized, we get

$$\mathbf{F}_{\text{fluid-solid}} = \sum_{i \in \text{fluid}} \sum_{j \in \text{solid}} (\mathbb{T}_j + \mathbb{T}_i) \cdot \nabla_i W_{ij} V_i V_j, \quad (10)$$

where i and j denote quantities associated with the fluid particles and the ghost particles respectively. One of the advantages of Eq. (10) is that it does not require interpolation on body nodes. For this reason, it is simpler and faster to use in practical applications. Since the inner summation of (10) approximates the divergence of the stress tensor, in practical simulations it is sufficient to substitute the corresponding operator of the SPH scheme at hand. In the present case, this leads to

$$\mathbf{F}_{\text{fluid-solid}} = \sum_{i \in \text{fluid}} \sum_{j \in \text{solid}} [-(p_j + p_i) + \rho_0 \nu \pi_{ij}] \nabla_i W_{ij} V_i V_j; \quad (11)$$

in which the first term on the right-hand side represents the pressure component and the second acts as the viscous component of the stress tensor.

The evaluation of the torque $\mathbf{T}_{\text{fluid-solid}}$ acting on the solid body can be derived by using the same approach shown above. Let us consider a fixed point \mathbf{r}_C . Then, the torque with respect to it is

$$\mathcal{T}_{\text{fluid-solid}} = \int_{\partial\Omega_s} (\mathbf{r} - \mathbf{r}_C) \times \langle \mathbb{T} \rangle \cdot \mathbf{n} dS, \quad (12)$$

and, following the procedure used for the evaluation of the force, it is possible to rearrange the above expression as follows:

$$\begin{aligned} \mathcal{T}_{\text{fluid-solid}} &= \int_{\Omega_f} dV \int_{\Omega_s} \{(\mathbf{r}^* - \mathbf{r}_C) \times [\mathbb{T} \cdot \nabla W(\mathbf{r}^* - \mathbf{r})] \\ &\quad + (\mathbf{r} - \mathbf{r}_C) \times [\mathbb{T}^* \cdot \nabla W(\mathbf{r}^* - \mathbf{r})]\} dV^* + \mathcal{O}(h). \end{aligned} \quad (13)$$

By analogy with formula (11), the above equation is discretized as follows:

$$\begin{aligned} \mathbf{T}_{\text{fluid-solid}} &= \sum_{i \in \text{fluid}} \sum_{j \in \text{solid}} \{(\mathbf{r}_j - \mathbf{r}_C) \times [(-p_i + \rho_0 \nu \pi_{ij}/2) \nabla_i W_{ij}] \\ &\quad + (\mathbf{r}_i - \mathbf{r}_C) \times [(-p_j + \rho_0 \nu \pi_{ij}/2) \nabla_i W_{ij}]\} V_i V_j. \end{aligned} \quad (14)$$

The expressions derived above for the force and torque are similar to those proposed in Monaghan et al. (2003) and Kajtar and Monaghan (2008). However, it is important to underline that, apart from the different enforcement of solid boundary conditions, in those cases the formulation is directly obtained from a momentum balance between the fluid and the repulsive body particles. Conversely, in the present case, the global loads are derived from the evaluation of the stress tensor on the body surface by means of a ghost fluid extension in the solid region.

4. Algorithm for handling fluid body coupling

The solid dynamics is modelled by the Newton's law of motion. Linear and Angular momentum equation are given in a simple 2-D framework by

$$\begin{cases} M \frac{d\mathbf{V}_G}{dt} = \mathbf{Mg} + \mathbf{F}_{\text{fluid-solid}}, \\ I_G \frac{d\Omega_G}{dt} = T_{\text{fluid-solid}}, \end{cases} \quad (15)$$

where \mathbf{V}_G and Ω_G are the velocity of the centre of gravity and the angular velocity of the body, M and I_G are the mass and the moment of inertia of the body around the centre of gravity and, finally, $\mathbf{F}_{\text{fluid-solid}}$ is the hydrodynamic force acting on the body. Here, $T_{\text{fluid-solid}}$ is the projection of the hydrodynamic torque along the unit vector \mathbf{k} normal to the plane, that is $T_{\text{fluid-solid}} = \mathbf{T}_{\text{fluid-solid}} \cdot \mathbf{k}$.

The dynamical state of the fluid particles, ghost particles and body nodes can be expressed through the vectors y_f , y_s and y_b respectively

$$\begin{aligned} y_f &= (\dots, \rho_i, \mathbf{u}_i, \mathbf{r}_i, \dots) \quad i \in \text{Fluid}, \\ y_s &= (\dots, \rho_j, \mathbf{u}_j, \mathbf{r}_j, \dots) \quad j \in \text{Solid}, \\ y_b &= (\dots, \mathbf{r}_k, \mathbf{u}_k, \mathbf{a}_k, \mathbf{n}_k, \dots) \quad k \in \text{Body Surface}. \end{aligned} \quad (16)$$

Further, the dynamical state of the rigid body is expressed by

$$y_g = (\mathbf{r}_G, \mathbf{V}_G, \theta_G, \Omega_G), \quad (17)$$

where \mathbf{r}_G and θ_G are respectively the position vector of the centre of gravity and the related angle of rotation.

The coupling between the two systems from Eqs. (1) and (15) can be represented by

$$\begin{cases} \dot{y}_f = \Phi_f(y_f, y_s, t), & y_f(t_0) = y_{f0}, \\ \dot{y}_g = \Phi_g(y_g, y_f, y_s, t), & y_g(t_0) = y_{g0}, \\ \dot{y}_s = \Phi_s(y_b, y_f, t), \\ y_b = \Phi_b(y_g, \dot{y}_g, y_{b0}), & y_{b0} = y_b(t_0), \end{cases} \quad (18)$$

where the symbol Φ represents a generic function and the last two equations represent, respectively, the dependence of the ghost state (Eqs. (3)–(5)) and of the body nodes state from the rigid motion equations.

The weakly compressible SPH equations march in time using an explicit scheme. Then, for the sake of simplicity, the whole system (18) follows the same time integration scheme. The 4th-order Runge Kutta algorithm offers a good balance between speed and stability and has been used for integrating the system of equations (18). In the latter the acceleration of the body appears on both sides of the equations. This is common in explicit schemes for fluid–body coupling. In potential flow solvers the body acceleration is generally taken into account through the added mass term (see e.g. Vinje and Breivig, 1981), enabling to move the body acceleration term from the right side to the left side. The added mass approach is also applied in other numerical solvers as an under-relaxation correction in the body motion (see e.g. Hǎdžić et al., 2005). Differently, in the present scheme the acceleration of the body on the right side is taken from the previous Runge–Kutta substep. This procedure is justified by the use of a very small time-step required by the weakly compressible assumption, as briefly recalled below.

At the generic time instant t^n , the state vector y_b is determined through y_g (predicted at the previous Runge–Kutta substep) and y_g . Then, the ghost fluid state y_s is obtained through the interpolation on the fluid particles, y_f , and the mirroring procedure (which requires y_b , as discussed in Section 3). The global loads $(\mathbf{F}, T)_{\text{fluid–solid}}$ are evaluated through Eqs. (10) and (14) and \dot{y}_g is obtained by (15). Finally, the interaction between fluid and ghost particles gives \dot{y}_f through Eq. (2). The iteration substep ends with the integration of y_g and \dot{y}_f to obtain respectively y_g and y_f at the time instant t^{n+1} .

As far as the time integration of system (18) is concerned, the time step has to account for the maximum acceleration (both body nodes and fluid particles) $|\mathbf{a}| = \max(\|\mathbf{a}_f\|_\infty, \|\mathbf{a}_b\|_\infty)$, the viscous diffusion and the sound speed

$$\Delta t \leq \min \left\{ \text{CFL}_1 \sqrt{\frac{h}{|\mathbf{a}|}}, \text{CFL}_2 \frac{h^2}{\nu}, \text{CFL}_3 \min_i \left[\frac{h}{c_0 + h \max_j \pi_{ij}} \right] \right\}, \quad (19)$$

with the first two time-step bounds obtained following Morris et al. (1997), while the third limit is derived following Monaghan and Kos (1999). For a fourth-order Runge–Kutta scheme and for the renormalized Gaussian kernel, the following CFL coefficients are heuristically found: $\text{CFL}_1 \leq 0.25$, $\text{CFL}_2 \leq 0.125$ and $\text{CFL}_3 \leq 2.0$, which ensure the stability of system (18).

5. Numerical tests and validation of the proposed algorithm

In this section five different test cases are discussed. The first one deals with a diffraction test in which a fixed body interacts with a regular wave system. For this problem experimental data for the forces and torque acting on the body are available and are used for the validation of the loads on bodies, crucial for the fluid–body coupling algorithm.

The second problem is dedicated to check the capability of the numerical model in maintaining in time the equilibrium of a simple floating body. In particular, it is shown that increasing the number of particles numerical errors on the body motions reduce.

In the third test case the robustness of the ghost–fluid technique discussed in Section 3 is inspected by studying the time evolution of a complex floating body dropped in a water tank. It is also shown that the floating body reaches the correct static equilibrium at the end of the transient stage.

The fourth test deals with a simple floating box with a non-uniform mass distribution. At the initial conditions the box is not in equilibrium and, consequently, it starts oscillating for several cycles around its equilibrium position. The convergence of the numerical scheme is studied and an analysis is performed about the mechanical energy exchange between the floating box and the fluid.

In the final test case, the problem of a wave packet interacting with a floating box is studied. For this case the proposed ghost–fluid technique has been validated against the experimental data available in the literature.

5.1. Diffraction test on a semi-immersed triangular body

Eqs. (10) and (14) are tested on a 2-D diffraction test case based on the experiments of Vugts (1968). The V-shape body (bottom angle of 60° and breadth at waterline $B=0.4$ m) is chosen for this test. The setup of the numerical test case is given in Fig. 4. The wave maker generates waves that propagate along the channel until they reach the triangular body where the forces and torques are measured. The NWT has to be long enough in order to reach a steady-state oscillatory regime of the forces and moments acting on the shape and avoid spurious reflections at the end of the tank. The depth has to be more than half the wavelength in order to simulate deep water waves.

Seven tests have been done in a wide range of frequencies, namely $2.8 < \lambda < 17$. The steepness of the generated wave is fixed at $kA=0.05$ but, for the calculus of the non-dimensional results, the effective value of the amplitude/steepness is taken into account. The signals of the force and torque are characterized by quasi-harmonic oscillations over a mean value. Fig. 5 displays the amplitude of these oscillations for the components of the force and the torque and the comparison with the experiments of Vugts (1968). When concerning the torque, the V-Shaped body gives rise to an asymmetric oscillation at $kA=0.05$. In this case, the value reported in Fig. 5 corresponds to the maximum displacement with respect to the mean value.

The overall agreement is fair though some discrepancies can be noticed. As a further check, an inspection of nonlinear effects on the V-shaped body would be necessary. However, in the experiments of Vugts (1968), the steepness of the incoming wave is not reported.

5.2. Floating body in rest condition

The aim of this case is to check the stability of a 2-D floating box initially disposed in a tank in a equilibrium condition. The body is a 2-D box of breadth $0.8L$ and height $0.4L$. The centre of gravity G of the body is the centre of the geometric figure. The box is initially half-submerged ($0.2L$), therefore the wetted perimeter is half the perimeter of the box. The mass $\rho \cdot 0.16L^2$ set the gravity forces equal to the buoyancy forces. The tank is large $L_{\text{tank}} = 5L$ and the filling height is fixed to $H_{\text{tank}} = 0.7L$. This trivial floating test is used to verify the stability of the algorithm, since the floating condition at rest generally spurs the development of instabilities, especially close to corners. Furthermore, it often represents the first part of a simulation involving water waves generated in a tank. Indeed, the box has to hold steady before the first wave comes.

The results are shown in Fig. 6 for three discretizations. The vertical displacement shows a maximum of order $\mathcal{O}(\Delta x)$ (comparable with the spacing between particles) that is acceptable. For the roll motion, the spurious motion is of order 0.1° for the coarser particles distribution and reduces by increasing the spatial resolution.

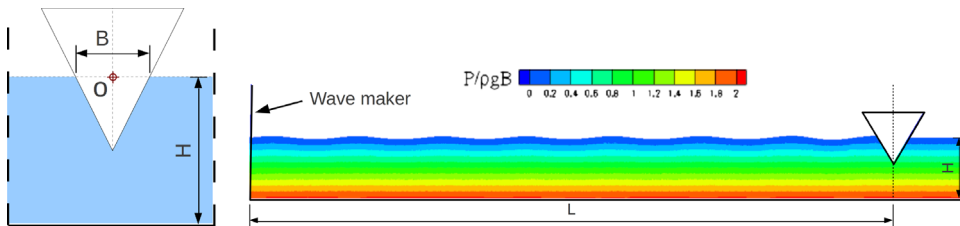


Fig. 4. Sketch of the 2-D diffraction test case by Vugts (1968).

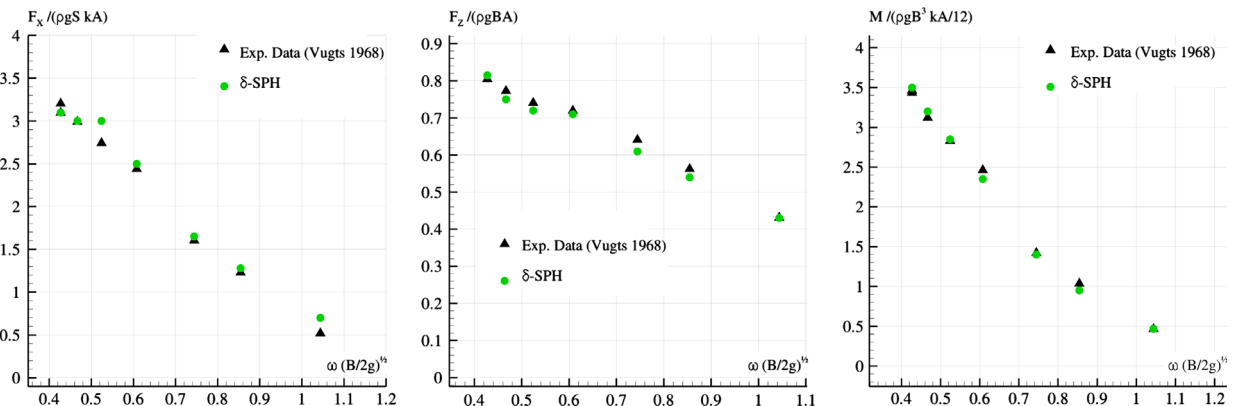


Fig. 5. Amplitude of the oscillations of the wave forces and torque for the diffraction test case: sway (left), heave (centre) and roll motion (right).

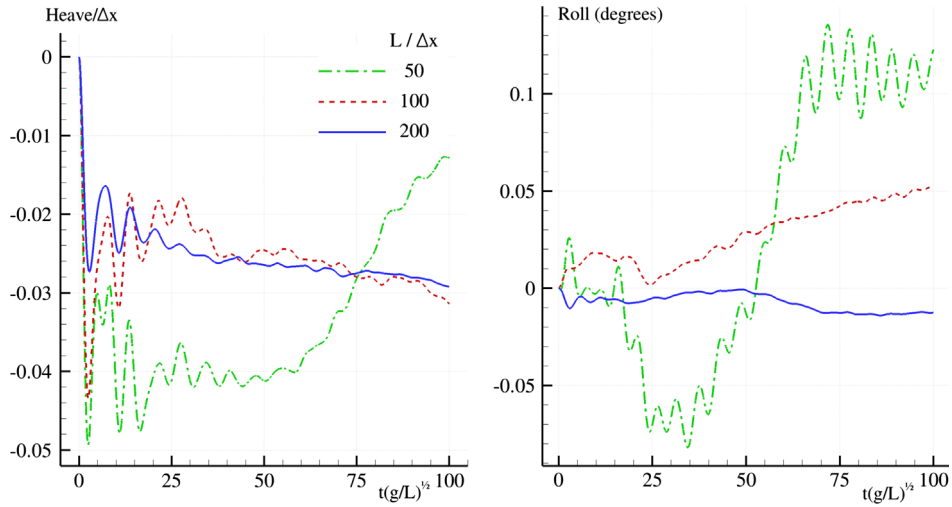


Fig. 6. Stability of 2-D box at equilibrium in buoyancy condition: heave (left) and roll motion (right).

Note that the spurious roll and heave motions are caused by an unavoidable small asymmetry in the initial particle positions. In any case, the fluid–body system always reaches a stable equilibrium configuration. Specifically, the discrepancies with respect to the exact equilibrium configuration are compatible with the adopted discretizations, confirming the stability of the proposed algorithm.

5.3. Drop of a complex floating body in a water tank

In this section a floating body characterized by a complex 2-D geometry is considered. The geometry together with the axis and the origin are depicted in the left upper plot of Fig. 7 for the initial condition. The body surface presents no symmetry planes and is composed by different curved patches (both concave and convex) that connect twelve corners. The mass of the body has been set equal to $M = 0.1483\rho L^2$ (where ρ is density of the fluid). The center of gravity, G , is positioned in the aft part of the body and its coordinates are $G = [0.2683L, 0.4352L]$. The moment of inertia with respect to G is $I_G = 0.01\rho L^4$. The Reynolds number (namely, $Re = L\sqrt{gL}/\nu$) is equal to 2000.

The chosen values of G and M ensure that only one stable equilibrium configuration exists. This theoretical equilibrium configuration, described by the rotation $\theta_G(\infty)$ and the immersion of the center of gravity $y_G/L(\infty)$, have been determined through a semi-analytical approach. In particular the body surface has been discretized and the hydrostatic pressures integrated along the profile to obtain the buoyancy forces. Then the couple $\theta_G(\infty)$ and $y_G/L(\infty)$ has been obtained through an iterative procedure and is the only one allowing for equilibrium between buoyancy forces and weight of the body. In the specific, the obtained values are $\theta_G(\infty) = 97.7^\circ$ (counter-clockwise positive) and $y_G/L(\infty) = 0.5098L$.

Starting from the initial condition, the body is dropped with zero velocity. Under the action of the gravity a complex water entry stage occurs (see plot upper plots of Fig. 7). The body then quickly rotates and sinks. In the meanwhile, an energetic wave motion takes place inside the tank (middle plots of Fig. 7). Due to the low viscosity adopted, the fluid motion is slowly damped in time (lower plots of Fig. 7). At $t = 100\sqrt{L/g}$ the fluid and the body are almost at rest condition. The time histories of the vertical position of G , y_G , and of the angle of rotation, θ_b , are reported in Fig. 8. These plots show that the present numerical scheme is able to reach the correct equilibrium after a complex fluid body interaction.

5.4. Oscillating floating box: convergence tests and energy conservation

In this section the long time evolution of a simple 2-D floating box is studied in detail. The sketch of the problem is depicted in Fig. 9. The water tank has a total length of $5L$ while the box is $0.8L \times 0.4L$. The centre of gravity, G , is shifted horizontally of $0.2L$ and, therefore, the box is not in equilibrium in the initial condition. The filling height of the tank, H , is equal to $0.7L$. Consequently, the tank bottom induces a relevant effect on the box motion, as well as on the wave irradiated. The mass of the box M is set equal to $M = 0.16\rho L^2$ (ρ is the fluid density), the momentum of inertia with respect G is $I_G = 0.01072\rho L^4$ and the Reynolds number ($Re = L\sqrt{gL}/\nu$) is 5000. Due to the large value of Re , a very fine spatial resolution is needed to correctly solve the boundary layer and capture the vortical structures developed during the evolution. Three spatial resolutions are adopted (namely, $L/\Delta x = 100, 200, 400$) to simulate a time evolution up to $t = 80\sqrt{L/g}$. A fourth test with $L/\Delta x = 800$ is performed but only for the first $20\sqrt{L/g}$ seconds. This fine spatial resolution requires 2 million particles and is used to show the evolution of the vorticity field in the first stage. The whole time evolution is driven by the initial potential energy of the box and the fluid (i.e. $E_0 = E_p^{\text{fluid}} + E_p^{\text{solid}}$). During the motion this is dissipated and converted into internal energy by the viscous forces. After the fluid and the body motions are extinguished, the box reaches the unique

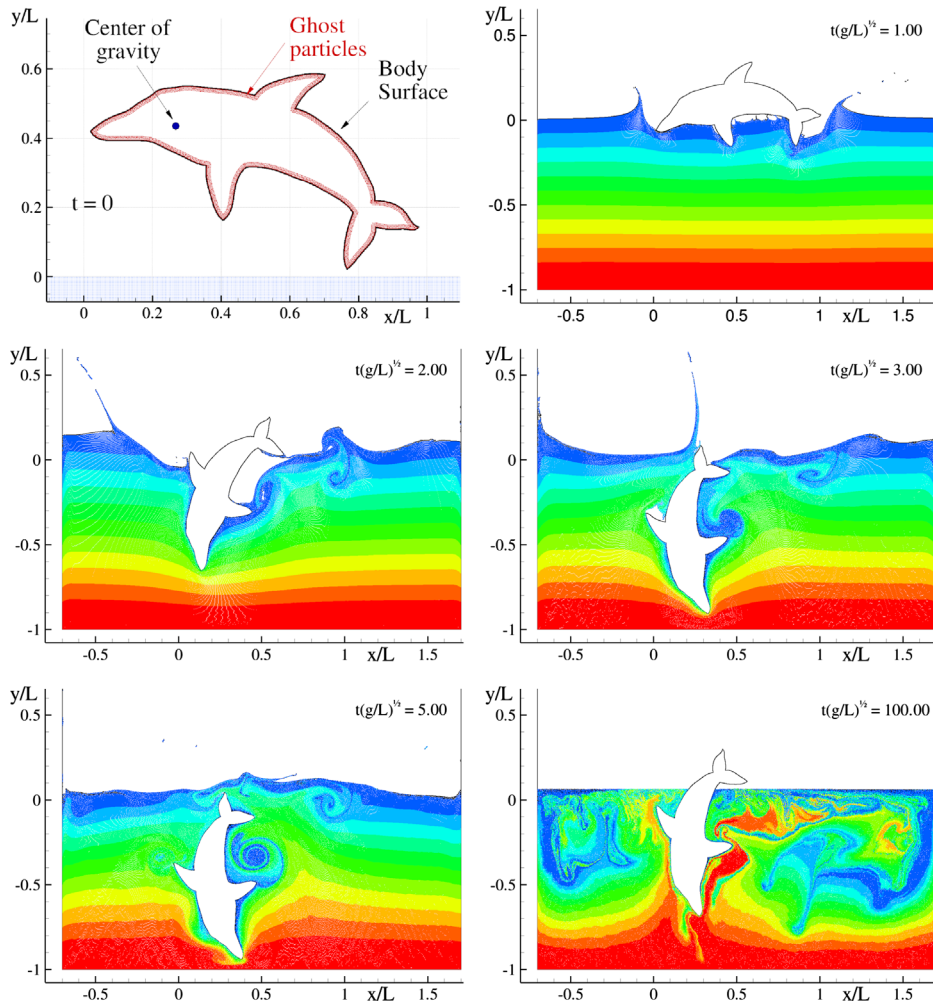


Fig. 7. Snapshots of the evolution of a complex floating body dropped in a water tank. The geometric details of the floating body are reported on the left upper plot. The particles are coloured according to their initial vertical positions.

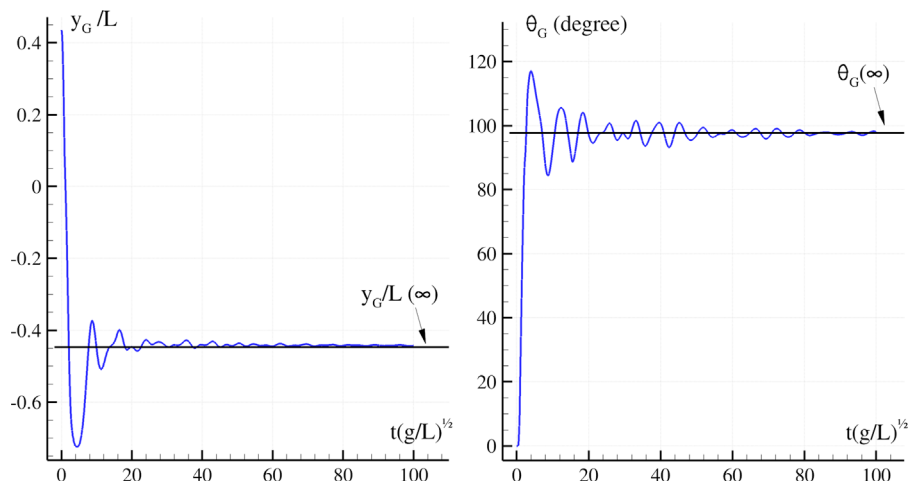


Fig. 8. Complex floating body dropped in a water tank. Left: time history of the vertical position of the centre of gravity G (left) and of the rotation around it (right).

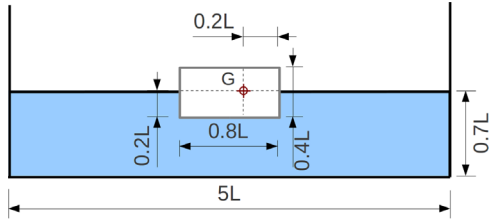


Fig. 9. Sketch of the 2-D test case with a freely floating box with a non-symmetric mass distribution.

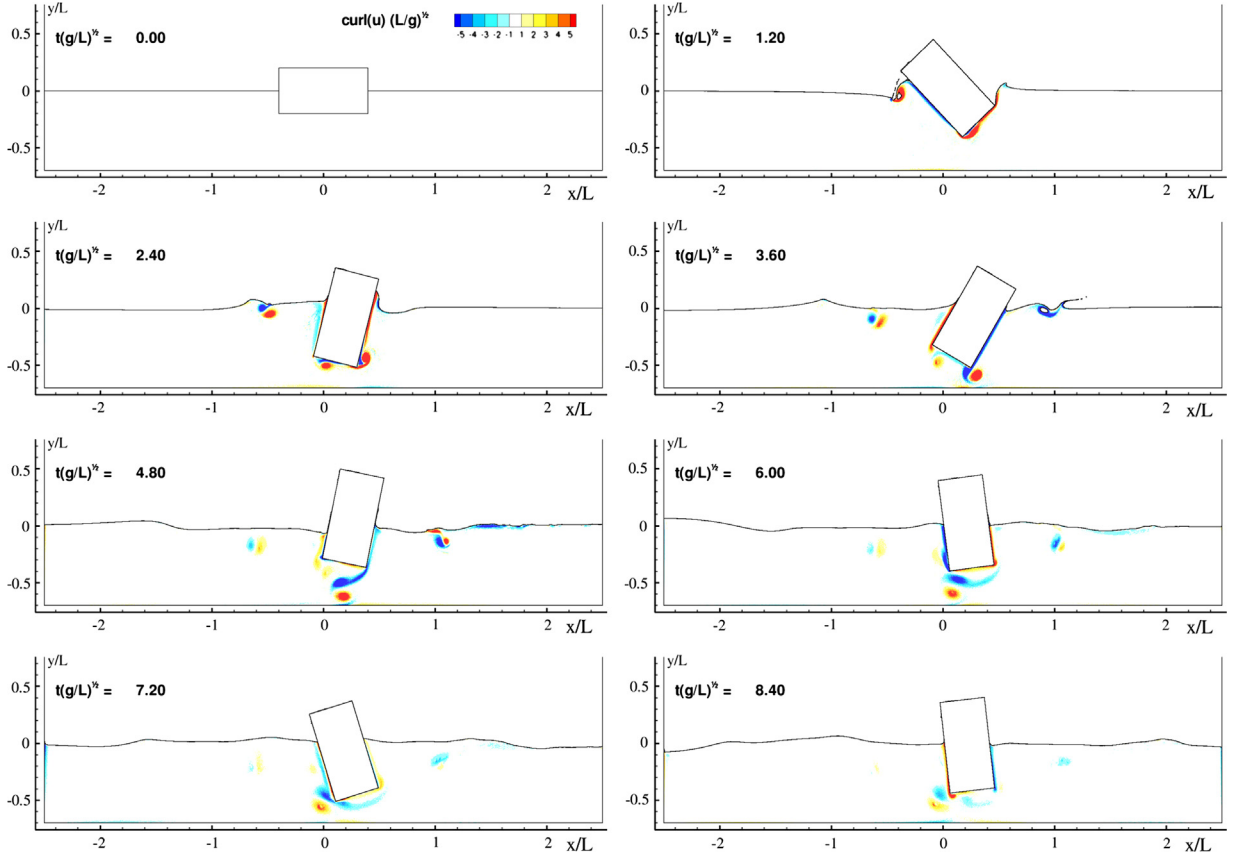


Fig. 10. Time evolution of the vorticity field for an oscillating floating box in a water tank ($L/\Delta x = 800$). Time increases left to right and top to bottom.

stable configuration, that is the vertical position with centre of gravity immersed by $0.2L$ under the free surface. In such configuration the variation of the potential energy of the box and the fluid is respectively $\Delta E_p^{\text{fluid}} = 0.1MgL$ and $\Delta E_p^{\text{solid}} = -0.2MgL$. Then, the whole dynamical system (i.e. body and fluid) dissipates an energy equal to $0.1MgL$.

Fig. 10 shows some snapshots of the time evolution with $L/\Delta x = 800$ (the colours indicate the intensity of the vorticity field). At the beginning of the simulation, the box starts rotating and, consequently, sheds vortices from the corners and irradiates waves that propagate back and forth within the tank. The vortical structures interact with the bottom of the tank, with the free surface, and couple in dipole structures moving in the fluid domain. In Fig. 11 two close views of the particle distribution and of the associated vorticity field are plotted at $t\sqrt{g/L} = 1.20$ for the finest resolution. These plots show that the boundary layer is well resolved at this discretization.

Fig. 12 shows the time histories of the floating box motion in its three degrees of freedom. The results are obtained by using three different spatial resolutions, namely $L/\Delta x = 100, 200, 400$. The results of Fig. 12 show that the data obtained with the highest resolution reach convergence. The time series $y_G(t)$ and $\theta_b(t)$ of Fig. 12 are used to evaluate, in L_2 norm, the distance between the results obtained with the different resolutions. The convergence rate lays between 1 and 2. This is the usual convergence rate for the δ -SPH model (see e.g. Antuono et al., 2010, 2011; Marrone et al., 2011a) and shows that the coupling with rigid body dynamics does not alter such a feature of the numerical scheme.

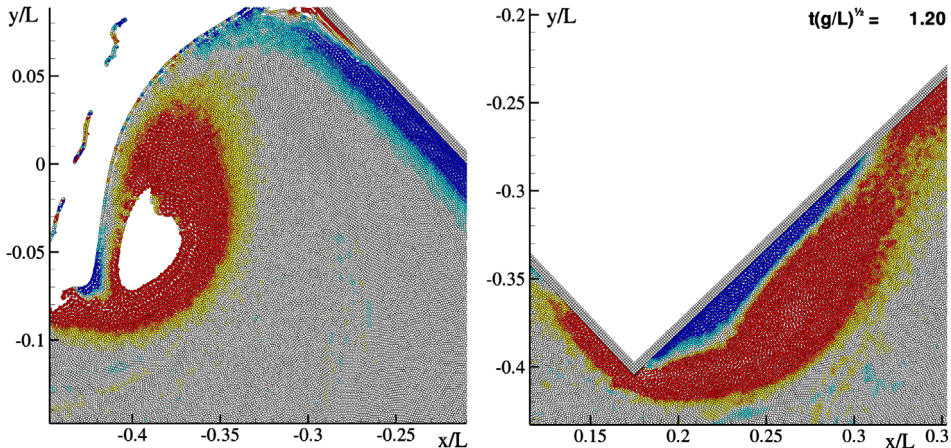


Fig. 11. Zoom of the particle configuration and vorticity field near the solid surface for the oscillating floating box test case at $t\sqrt{g/L} = 1.20$ for $L/\Delta x = 800$. Left: close view near the left wall. Right: close view of the immersed corner.

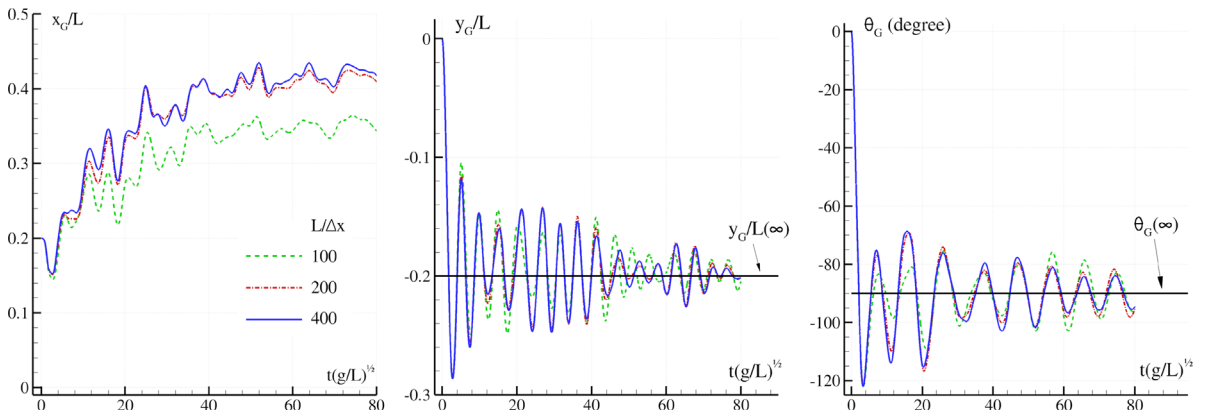


Fig. 12. Time evolution of a floating box in a water tank. Left: sway motion of the centre of gravity, x_G . Middle: heave motion, y_G . Right: roll angle around G , θ_b .

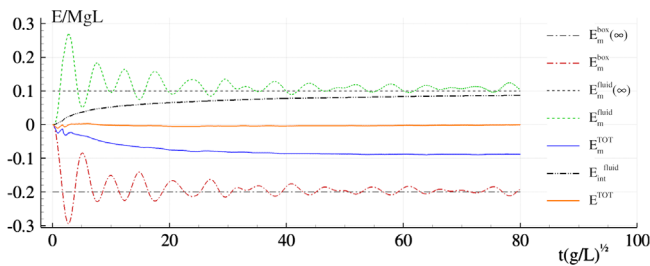


Fig. 13. Time evolution of a floating box in a water tank: mechanical energy of the fluid (E_m^{fluid} , dashed line), of the floating body (E_m^{box} , dash-dotted line) and of the internal energy of the fluid ($E_{\text{int}}^{\text{fluid}}$).

Finally, an analysis of the different energy contributions of the fluid-body system is performed. Fig. 13 shows the time evolution of the mechanical energy of the body, E_m^{box} , and of the fluid, E_m^{fluid} . Part of E_m^{box} is initially transferred to the fluid, inducing an increase of E_m^{fluid} , while the total mechanical energy of the fluid-box system, that is $E_m^{\text{TOT}} = E_m^{\text{box}} + E_m^{\text{fluid}}$, decreasing under the action of the viscous forces. The total energy of the system, i.e. $E^{\text{TOT}} = E_{\text{int}}^{\text{fluid}} + E_m^{\text{TOT}}$, should be zero since no external force is doing work on the fluid-box system. Fig. 13 shows that, remarkably, the present model ensures a good conservation of the total energy. This is not a trivial result as already discussed in Section 2.

5.5. Wave packet interacting with a floating body

In Hădžić et al. (2005) a detailed study of a floating body subjected to a wave packet was carried out. In particular, experimental data were obtained in a small towing tank of the Berlin University of Technology. The body was a rectangular

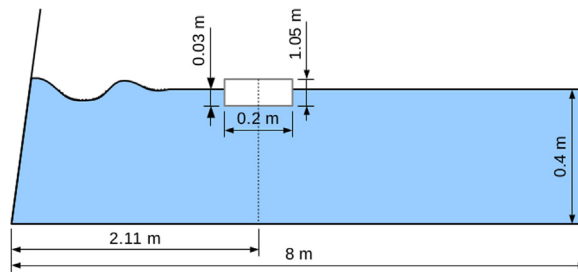


Fig. 14. 2-D sketch of the freely floating box interacting with a wave packet.

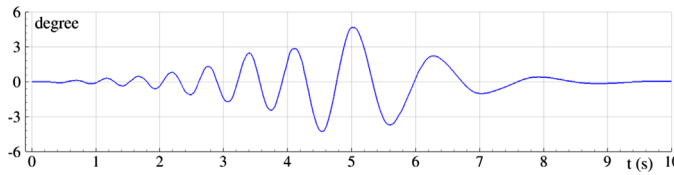


Fig. 15. Time history of the flap wavemaker angle used for the generation of a wave packet.

prism 10 cm wide, 5 cm high and 29 cm long, with density relative to water being 0.68. The body was located at $x=2.11$ m away from the wave-maker, whose motion was controlled to produce a wave packet with a focusing point at the original location of the body. Due to the long transversal dimension of the prism, the experiments can be regarded as two-dimensional. The time history of the three degrees-of-freedom were recorded during the interactions with the wave packet. A sketch of the problem is depicted in Fig. 14. The mass of the body is 0.986 kg while the moment of inertia is 14 kg cm^2 (the body is an aluminium box).

Fig. 15 shows the time history of the flap wavemaker angle used to generate the wave packet. This experimental condition is appropriate to validate the SPH capabilities in correctly reproducing the motion forced by the wave packet. At the focusing point the wave packet is quite steep and has an height equal to the body. Then, a nonlinear behaviour is observed in both the resulting wave evolution and the body motion.

In Antuono et al. (2011) the present δ -SPH scheme was already validated on the generation and propagation of wave packets. In that work it was demonstrated that the ratio between the wave amplitude and the particle size, $A/\Delta x$, has to be of order of 10 to avoid overdamping. In the present test case the resolution adopted is $A/\Delta x=40$, that is, sufficient to correctly model the wave packet in the numerical tank. About 2 millions of particles have been used with this spatial resolution.

During the experiments the wave elevation was recorded by two fixed probes at $x=1.65$ m and $x=2.66$ m (see Fig. 17). Fig. 16 shows the comparison between SPH and the time histories of the two wave elevations recorded, confirming the correct generation/propagation of the wave packet.

Two snapshots of the free-surface deformation and position of the floating body at time $t=7.2$ s and $t=7.59$ s are depicted in Fig. 17 while Fig. 18 shows an enlarged view of the floating box at the same time instants. The comparison with the two experimental pictures shows a good match between the SPH solution and the experiments during the interaction between the wave packet and the floating body.

Finally, in Fig. 19 the SPH time histories of the floating body motions are compared with the experimental data.

6. Conclusions

A SPH solver is developed for applications in the framework of NWT (Numerical Wave Tanks) and floating bodies. To this aim, a complete algorithm able to compute viscous and fully coupled fluid solid interactions is described.

A no-slip boundary condition on the solid surface is enforced through a ghost-fluid technique. For the considered problem, the intersection between the free surface and the solid profile has to be carefully addressed. The details of a specific treatment regarding the ghost fluid close to the free surface are described. Further, a formula for the evaluation of forces and torque is also provided in the ghost-fluid framework. The assessment of loads acting on bodies is validated through a difficult diffraction test case with satisfactory results.

An explicit algorithm is developed for the full coupling between fluid and rigid bodies. Stability, convergence and conservation properties are tested on several freely floating test cases and a final validation of the full algorithm is performed for the interaction between a 2-D box and an incoming wave packet.

It has been proved that the proposed model can solve complex viscous flows (involving floating bodies) with a good accuracy. Starting from this point, further developments are needed to optimize the SPH for this kind of applications,

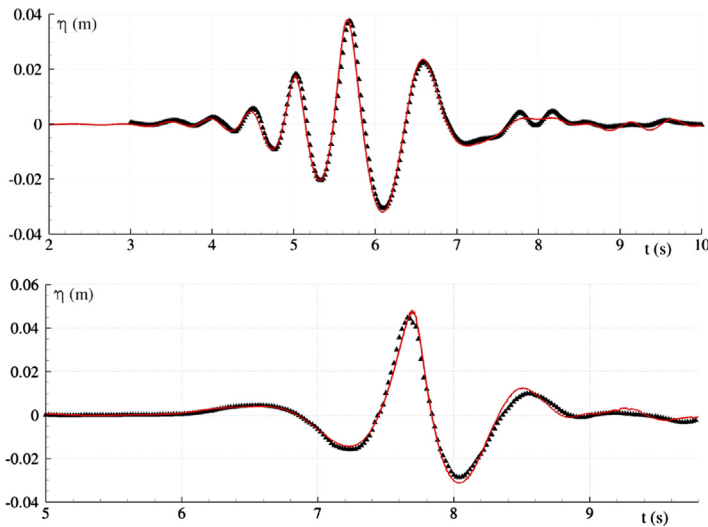


Fig. 16. Time histories of the wave elevation during the evolution of the wave packet (SPH, solid line; experimental data, \blacktriangle). Top: $x=1.65$ m. Bottom $x=2.66$ m.

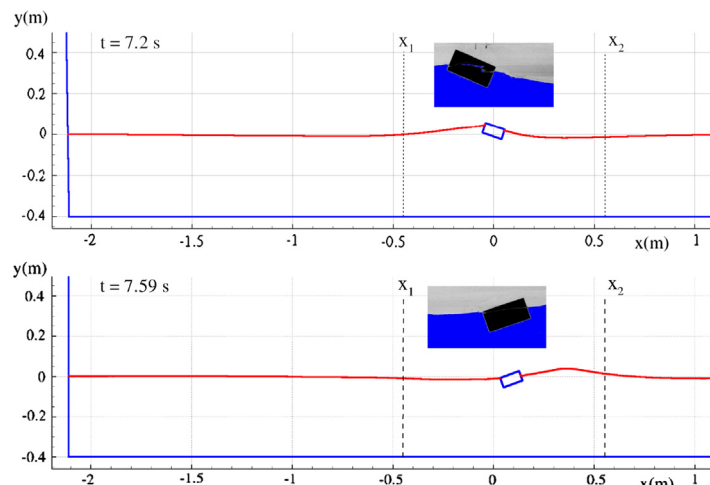


Fig. 17. Free-surface deformation and position the floating body at $t=7.2$ s (top) and $t=7.59$ s (bottom). Pictures of the experiments are reported on the top part of the plots. The wave probes positions x_1 and x_2 are also reported.

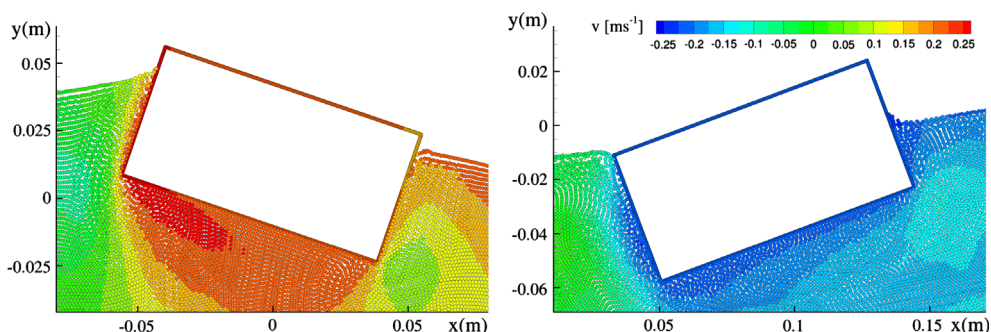


Fig. 18. Enlarged view of the floating body at $t=7.2$ s (left) and $t=7.59$ s (Right). The particles are coloured according to their vertical velocities. (For interpretation of the references to color in this figure caption, the reader is referred to the web version of this paper.)

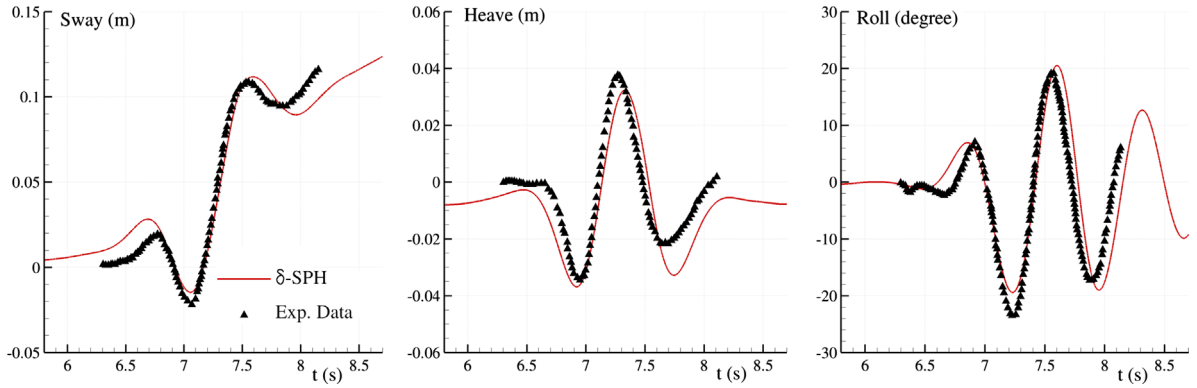


Fig. 19. Time histories of the floating body motions during the interaction with the wave packet (SPH, solid line; experimental data, ▲).

especially in the 3D context. For this purposes multi-spatial resolution models are needed and this topic is left for future works.

Acknowledgements

The research leading to these results has received funding by the Flagship Project RITMARE – The Italian Research for the Sea – coordinated by the Italian National Research Council and funded by the Italian Ministry of Education, University and Research within the National Research Program 2011–2013. It has been also partially funded by the European Community's Seventh Framework Programme.

Appendix A. Derivation of formulas for the evaluation of forces and torques

Denoting by $\langle \mathbb{T} \rangle$ the smoothed stress tensor, the global force on the body is

$$\mathcal{F}_{\text{fluid-solid}} = \int_{\partial\Omega_s} \langle \mathbb{T} \rangle \cdot \mathbf{n} \, dS, \quad (\text{A.1})$$

where \mathbf{n} is the unit outward normal to the solid profile. Assuming the flow field to be mirrored on the solid body through a proper ghost–fluid technique, the stress tensor can be decomposed in

$$\langle \mathbb{T} \rangle(\mathbf{r}) = \int_{\Omega_f} \mathbb{T}' W(\mathbf{r}' - \mathbf{r}) \, dV' + \int_{\Omega_s} \mathbb{T}^* W(\mathbf{r}^* - \mathbf{r}) \, dV^*, \quad (\text{A.2})$$

where the starred variables indicate quantities mirrored over the solid domain Ω_s . Substituting (A.2) into (A.1), we obtain

$$\begin{aligned} \mathcal{F}_{\text{fluid-solid}} &= \int_{\partial\Omega_s} dS \mathbf{n} \cdot \int_{\Omega_f} \mathbb{T}' W(\mathbf{r}' - \mathbf{r}) \, dV' + \int_{\partial\Omega_s} dS \mathbf{n} \cdot \int_{\Omega_s} \mathbb{T}^* W(\mathbf{r}^* - \mathbf{r}) \, dV^* \\ &= \int_{\Omega_f} dV' \mathbb{T}' \cdot \int_{\partial\Omega_s} \mathbf{n} W(\mathbf{r}' - \mathbf{r}) \, dS + \int_{\Omega_s} dV^* \mathbb{T}^* \cdot \int_{\partial\Omega_s} \mathbf{n} W(\mathbf{r}^* - \mathbf{r}) \, dS. \end{aligned} \quad (\text{A.3})$$

Further, using the divergence theorem and the kernel properties, we can write

$$\begin{aligned} \int_{\partial\Omega_s} \mathbf{n} W(\mathbf{r}' - \mathbf{r}) \, dS &= - \int_{\partial\Omega_s} \mathbf{n}^{(S)} W(\mathbf{r}' - \mathbf{r}) \, dS = - \int_{\Omega_s} \nabla^* W(\mathbf{r}' - \mathbf{r}^*) \, dV^*, \\ \int_{\partial\Omega_s} \mathbf{n} W(\mathbf{r}^* - \mathbf{r}) \, dS &= \int_{\Omega_f} \nabla W(\mathbf{r}^* - \mathbf{r}) \, dV + \int_{\Omega_0} \nabla W(\mathbf{r}^* - \mathbf{r}) \, dV \\ &= \int_{\Omega_f} \nabla W(\mathbf{r}^* - \mathbf{r}) \, dV - \int_{\Omega_0} \nabla^* W(\mathbf{r}^* - \mathbf{r}) \, dV, \end{aligned} \quad (\text{A.4})$$

where $\mathbf{n}^{(S)}$ is the normal vector pointing outwards the solid domain (i.e. inwards the fluid domain) while the subscript '0' indicates the void region Ω_0 which has to be eventually included when the kernel domain intersects the free surface. In the sequel, we show that the contribution due to Ω_0 is always of order $\mathcal{O}(h)$ and, consequently, it can be neglected. For the sake of the notation, we simply write

$$\int_{\Omega_0} \nabla^* W(\mathbf{r}^* - \mathbf{r}) \, dV = \nabla^* \Gamma_0(\mathbf{r}^*). \quad (\text{A.5})$$

Substituting the identities derived in (A.4) into (A.3), we obtain

$$\mathcal{F}_{\text{fluid-solid}} = - \int_{\Omega_f} dV' \mathbb{T}' \cdot \int_{\Omega_s} \nabla^* W(\mathbf{r}' - \mathbf{r}^*) dV^* + \int_{\Omega_s} dV^* \mathbb{T}^* \cdot \int_{\Omega_f} \nabla W(\mathbf{r}^* - \mathbf{r}) dV - \int_{\Omega_s} \mathbb{T}(\mathbf{r}^*) \cdot \nabla^* \Gamma_0(\mathbf{r}^*) dV^*. \quad (\text{A.6})$$

Let us focus on the first two integrals. It follows:

$$\begin{aligned} & - \int_{\Omega_f} dV' \mathbb{T}' \cdot \int_{\Omega_s} \nabla^* W(\mathbf{r}' - \mathbf{r}^*) dV^* + \int_{\Omega_s} dV^* \mathbb{T}^* \cdot \int_{\Omega_f} \nabla W(\mathbf{r}^* - \mathbf{r}) dV \\ &= - \int_{\Omega_f} dV \mathbb{T} \cdot \int_{\Omega_s} \nabla^* W(\mathbf{r}^* - \mathbf{r}) dV^* + \int_{\Omega_s} dV^* \mathbb{T}^* \cdot \int_{\Omega_f} \nabla W(\mathbf{r}^* - \mathbf{r}) dV \\ &= \int_{\Omega_f} dV \int_{\Omega_s} [\mathbb{T}^* \cdot \nabla W(\mathbf{r}^* - \mathbf{r}) - \mathbb{T} \cdot \nabla^* W(\mathbf{r}^* - \mathbf{r})] dV^* \\ &= \int_{\Omega_f} dV \int_{\Omega_s} (\mathbb{T}^* + \mathbb{T}) \cdot \nabla W(\mathbf{r}^* - \mathbf{r}) dV^*. \end{aligned}$$

Then, the final expression for global force on the solid body is

$$\mathcal{F}_{\text{fluid-solid}} = \int_{\Omega_f} dV \int_{\Omega_s} (\mathbb{T}^* + \mathbb{T}) \cdot \nabla W(\mathbf{r}^* - \mathbf{r}) dV^* - \int_{\Omega_s} \mathbb{T}(\mathbf{r}^*) \cdot \nabla^* \Gamma_0(\mathbf{r}^*) dV^*. \quad (\text{A.7})$$

Now, let us focus on the last term in (A.7). Note that $\nabla^* \Gamma_0$ can be rewritten as follows:

$$\nabla^* \Gamma_0(\mathbf{r}^*) = \int_{\partial\Omega_0} \mathbf{n}^{(0)} W(\mathbf{r}^* - \mathbf{r}_0) dS_0, \quad (\text{A.8})$$

where $\mathbf{n}^{(0)}$ is the unit vector normal to the free surface pointing outwards of the fluid region. Then, using a Taylor expansion, we can write

$$\begin{aligned} \mathbb{T}(\mathbf{r}^*) \cdot \nabla \Gamma_0(\mathbf{r}^*) &= \int_{\partial\Omega_0} \mathbb{T}(\mathbf{r}^*) \cdot \mathbf{n}^{(0)} W(\mathbf{r}^* - \mathbf{r}_0) dS_0 \\ &= \int_{\partial\Omega_0} \left[\mathbb{T}_{ij}(\mathbf{r}_0) + \left(\frac{\partial \mathbb{T}_{ij}}{\partial r_k} \right) \Big|_{\mathbf{r}^*} (r^* - r_0)_k + \mathcal{O}(\|\mathbf{r}^* - \mathbf{r}_0\|^2) \right] n_j^{(0)} W(\mathbf{r}^* - \mathbf{r}_0) dS_0 \\ &= \left(\frac{\partial \mathbb{T}_{ij}}{\partial r_k} \right) \Big|_{\mathbf{r}^*} \int_{\partial\Omega_0} (r^* - r_0)_k n_j^{(0)} W(\mathbf{r}^* - \mathbf{r}_0) dS_0 + \mathcal{O}(h), \end{aligned} \quad (\text{A.9})$$

since, by definition, along the free surface the tension is null, i.e., $\mathbb{T}(\mathbf{r}_0) \cdot \mathbf{n}_0 = 0$. To complete the derivation, we have to prove that

$$\int_{\partial\Omega} (\mathbf{r}' - \mathbf{r}) \otimes \mathbf{n}' W(\mathbf{r}' - \mathbf{r}) dS' = \mathcal{O}(h), \quad (\text{A.10})$$

where $\partial\Omega$ is a generic closed surface. Using the Gauss–Green relation and the kernel properties, we obtain

$$\int_{\partial\Omega} (\mathbf{r}' - \mathbf{r}) \otimes \mathbf{n}' W(\mathbf{r}' - \mathbf{r}) dS' = \Gamma(\mathbf{r}) \mathbb{1} - \int_{\Omega} (\mathbf{r}' - \mathbf{r}) \otimes \nabla W(\mathbf{r}' - \mathbf{r}) dV', \quad (\text{A.11})$$

where $\mathbb{1}$ is the identity matrix and

$$\Gamma(\mathbf{r}) = \int_{\Omega} W(\mathbf{r}' - \mathbf{r}) dV'. \quad (\text{A.12})$$

Because of the kernel properties, it is simple to show that

$$\int_{\Omega} (\mathbf{r}' - \mathbf{r}) \otimes \nabla W dV' = \Gamma(\mathbf{r}) \mathbb{1} + \mathcal{O}(h), \quad (\text{A.13})$$

and this proves (A.10). Finally, substituting (A.10) in (A.9), we obtain

$$\mathbb{T}(\mathbf{r}^*) \cdot \nabla \Gamma_0(\mathbf{r}^*) = \mathcal{O}(h). \quad (\text{A.14})$$

Actually, the global contribute related to the free surface is even smaller since $\mathbb{T}(\mathbf{r}^*) \equiv 0$ when $\Omega_f(\mathbf{r}^*) = \emptyset$. In any case, we can write

$$\mathcal{F}_{\text{fluid-solid}} = \int_{\Omega_f} dV \int_{\Omega_s} (\mathbb{T}^* + \mathbb{T}) \cdot \nabla W(\mathbf{r}^* - \mathbf{r}) dV^* + \mathcal{O}(h). \quad (\text{A.15})$$

Now, we proceed to evaluate the torque on the solid body. Let \mathbf{r}_C be a fixed point; then, the torque with respect to the point \mathbf{r}_C is

$$\mathcal{T} = \int_{\partial\Omega_s} (\mathbf{r} - \mathbf{r}_C) \times (\mathbb{T} \cdot \mathbf{n}) dS \Rightarrow \mathcal{T}_i = \int_{\partial\Omega_s} \epsilon_{ijk} (r - r_C)_j \mathbb{T}_{kl} n_l dS,$$

where ϵ_{ijk} is the Ricci's tensor. Similarly to the formula for the force, we adapt the above expression to the SPH framework and write

$$\mathcal{T}_i = \int_{\partial\Omega_s} \epsilon_{ijk}(r-r_C)_j \langle \mathbb{T} \rangle_{kl} n_l dS, \quad (\text{A.16})$$

and $\langle \mathbb{T} \rangle$ is given by (A.2). After substitution, we get

$$\begin{aligned} \mathcal{T}_i &= \int_{\partial\Omega_s} dS \epsilon_{ijk}(r-r_C)_j n_l \int_{\Omega_f} \mathbb{T}'_{kl} W(\mathbf{r}'-\mathbf{r}) dV' + \int_{\partial\Omega_s} dS \epsilon_{ijk}(r-r_C)_j n_l \int_{\Omega_s} \mathbb{T}_{kl}^* W(\mathbf{r}^*-\mathbf{r}) dV^* \\ &= \int_{\Omega_f} dV' \epsilon_{ijk} \mathbb{T}'_{kl} \int_{\partial\Omega_s} dS(r-r_C)_j n_l W(\mathbf{r}'-\mathbf{r}) + \int_{\Omega_s} dV^* \epsilon_{ijk} \mathbb{T}_{kl}^* \int_{\partial\Omega_s} dS(r-r_C)_j n_l W(\mathbf{r}^*-\mathbf{r}). \end{aligned}$$

Using the divergence theorem, we obtain

$$\begin{aligned} \int_{\partial\Omega_s} dS(r-r_C)_j n_l W(\mathbf{r}'-\mathbf{r}) &= - \int_{\partial\Omega_s} dS(r-r_C)_j n_l^{(S)} W(\mathbf{r}'-\mathbf{r}) \\ &= - \int_{\Omega_s} (r^*-r_C)_j \frac{\partial W(\mathbf{r}'-\mathbf{r}^*)}{\partial r_l^*} dV^* - \delta_{jl} \int_{\Omega_s} W(\mathbf{r}'-\mathbf{r}^*) dV^* \\ &= - \int_{\Omega_s} (r^*-r_C)_j \frac{\partial W(\mathbf{r}'-\mathbf{r}^*)}{\partial r_l^*} dV^* - \delta_{jl} \Gamma_s(\mathbf{r}'), \end{aligned}$$

where $\mathbf{n}^{(S)}$ is the normal vector pointing outwards the solid domain (i.e. inwards the fluid domain) and δ_{jl} is the Kronecker delta. Similarly, we obtain

$$\int_{\partial\Omega_s} dS(r-r_C)_j n_l W(\mathbf{r}^*-\mathbf{r}) = \int_{\Omega_f} (r-r_C)_j \frac{\partial W(\mathbf{r}^*-\mathbf{r})}{\partial r_l} dV + \delta_{jl} \Gamma_f(\mathbf{r}^*), + \int_{\Omega_0} \frac{\partial}{\partial r_{0,l}} [(r_0-r_C)_j W(\mathbf{r}^*-\mathbf{r}_0)] dV_0, \quad (\text{A.17})$$

where accordingly to the notation at hand

$$\Gamma_f(\mathbf{r}^*) = \int_{\Omega_f} W(\mathbf{r}^*-\mathbf{r}) dV.$$

The last term on the right-hand side of (A.17) takes into account the influence of the free surface and, as proved in the following, is negligible. Since $\epsilon_{ijk} \mathbb{T}_{kl} \delta_{jl} = \epsilon_{ijk} \mathbb{T}_{kj}$ and \mathbb{T} is symmetric, it follows:

$$\epsilon_{ijk} \mathbb{T}_{kj} = \epsilon_{ikj} \mathbb{T}_{jk} = -\epsilon_{ijk} \mathbb{T}_{kj} \Rightarrow \epsilon_{ijk} \mathbb{T}_{kj} = 0, \quad (\text{A.18})$$

and, consequently, the terms containing Γ_f and Γ_s give a null contribute to the momenta. Then, we obtain

$$\begin{aligned} \mathcal{T}_i &= - \int_{\Omega_f} dV' \epsilon_{ijk} \mathbb{T}'_{kl} \int_{\Omega_s} (r^*-r_C)_j \frac{\partial W(\mathbf{r}'-\mathbf{r}^*)}{\partial r_l^*} dV^* + \int_{\Omega_s} dV^* \epsilon_{ijk} \mathbb{T}_{kl}^* \int_{\Omega_f} (r-r_C)_j \frac{\partial W(\mathbf{r}^*-\mathbf{r})}{\partial r_l} dV \\ &= \int_{\Omega_f} dV' \epsilon_{ijk} \mathbb{T}'_{kl} \int_{\Omega_s} (r^*-r_C)_j \frac{\partial W(\mathbf{r}'-\mathbf{r}^*)}{\partial r_l'} dV^* + \int_{\Omega_s} dV^* \epsilon_{ijk} \mathbb{T}_{kl}^* \int_{\Omega_f} (r-r_C)_j \frac{\partial W(\mathbf{r}^*-\mathbf{r})}{\partial r_l} dV \\ &= \int_{\Omega_f} dV \epsilon_{ijk} \mathbb{T}_{kl} \int_{\Omega_s} (r^*-r_C)_j \frac{\partial W(\mathbf{r}-\mathbf{r}^*)}{\partial r_l} dV^* + \int_{\Omega_s} dV^* \epsilon_{ijk} \mathbb{T}_{kl}^* \int_{\Omega_f} (r-r_C)_j \frac{\partial W(\mathbf{r}^*-\mathbf{r})}{\partial r_l} dV \\ &= \int_{\Omega_f} dV \int_{\Omega_s} \epsilon_{ijk} [(r^*-r_C)_j \mathbb{T}_{kl} + (r-r_C)_j \mathbb{T}_{kl}^*] \frac{\partial W(\mathbf{r}^*-\mathbf{r})}{\partial r_l} dV^*. \end{aligned}$$

This formula can be rewritten as follows:

$$\mathcal{T}_i = \int_{\Omega_f} dV \int_{\Omega_s} \{(\mathbf{r}^*-\mathbf{r}_C) \times [\mathbb{T} \cdot \nabla W(\mathbf{r}^*-\mathbf{r})] + (\mathbf{r}-\mathbf{r}_C) \times [\mathbb{T}^* \cdot \nabla W(\mathbf{r}^*-\mathbf{r})]\} dV^*.$$

Now, we prove that the free-surface contribution is negligible, that is

$$\int_{\Omega_s} dV^* \epsilon_{ijk} \mathbb{T}_{kl}^* \int_{\Omega_0} \frac{\partial}{\partial r_{0,l}} [(r_0-r_C)_j W(\mathbf{r}^*-\mathbf{r}_0)] dV_0 = \mathcal{O}(h). \quad (\text{A.19})$$

First, using the divergence theorem, we rewrite this term as follows:

$$\int_{\Omega_s} dV^* \int_{\partial\Omega_0} \epsilon_{ijk} (r_0-r_C)_j \mathbb{T}_{kl}^{(0)} n_l^{(0)} W(\mathbf{r}^*-\mathbf{r}_0) dV_0 = \int_{\Omega_s} dV^* \int_{\partial\Omega_0} (\mathbf{r}_0-\mathbf{r}_C) \times (\mathbb{T}^* \cdot \mathbf{n}_0) W(\mathbf{r}^*-\mathbf{r}_0) dV_0.$$

Then, using a Taylor expansion, we find

$$\mathbb{T}(\mathbf{r}^*) = \mathbb{T}(\mathbf{r}_0) + \mathcal{O}(h) \Rightarrow \mathbb{T}(\mathbf{r}^*) \cdot \mathbf{n}_0 = \mathcal{O}(h), \quad (\text{A.20})$$

since, by definition, $\mathbb{T}(\mathbf{r}_0) \cdot \mathbf{n}_0 = 0$. This proves that (A.19) holds true.

References

- Antuono, M., Colagrossi, A., Marrone, S., Molteni, D., 2010. Free-surface flows solved by means of SPH schemes with numerical diffusive terms. *Computer Physics Communications* 181, 532–549.
- Antuono, M., Colagrossi, A., Marrone, S., Lugni, C., 2011. Propagation of gravity waves through a SPH schemes with numerical diffusive terms. *Computer Physics Communications* 182, 866–877.
- Benz, W., 1989. Smooth particle hydrodynamics: a review, Harvard-Smithsonian Center for Astrophysics, Preprint Series No. 2884.
- Broglia, R., Bouscasse, B., Di Mascio, A., Lugni, C., 2009. Experimental and numerical analysis of the roll decay motion for a patrol boat. In: Proceeding of the 19th International Offshore and Polar Engineering Conference (ISOPE), Osaka (Japan).
- Colagrossi, A., Landrini, M., 2003. Numerical simulation of interfacial flows by Smoothed Particle Hydrodynamics. *Journal of Computational Physics* 191, 448–475.
- Colagrossi, A., Antuono, M., Souto-Iglesias, A., Le Touzé, D., 2011. Theoretical analysis and numerical verification of the consistency of viscous smoothed-particle-hydrodynamics formulations in simulating free-surface flows. *Physical Review E* 84, 026705. [13 pages].
- Colagrossi, A., Bouscasse, B., Antuono, M., Marrone, S., 2012. Particle packing algorithm for SPH schemes. *Computer Physics Communications* 183 (8), 1641–1653.
- De Leffe, M., Le Touzé, D., Alessandrini, B., 2011. A modified no-slip condition in weakly-compressible SPH. In: Proceeding of the Sixth International SPHERIC Workshop, 8–10 June 2011, Hamburg, Germany.
- Delorme, L., Bulian, G., Mc Cue, L., Souto-Iglesias, A., 2006. Coupling between sloshing and ship roll motion: comparison between nonlinear potential theory and SPH. In: Proceeding of the 26th Symposium on Naval Hydrodynamics, Rome, Italy.
- Di Mascio, A., Broglia, R., Muscari, R., 2008. Numerical simulations of viscous flow around a naval combatant in regular head waves. In: Proceeding of the Sixth Osaka Colloquium on Seakeeping and Stability of Ships, Osaka, Japan.
- Doring, M., 2005. Développement d'une méthode SPH pour les applications à surface libre en hydrodynamique. Ph.D. Thesis, Ecole Centrale de Nantes.
- Eightesad, A., Shafei, A.R., Mahzoon, M., 2012. A new fluid–solid interface algorithm for simulating fluid structure problems in FGM plates. *Journal of Fluids and Structures* 30, 141–158.
- Faltinsen, O.M., 1977. Numerical solutions of transient nonlinear free-surface motion outside or inside moving bodies. In: Proceedings of the Second International Conference on Numerical Ship Hydrodynamics, University of California, Berkeley, Extension Publications, pp. 347–357.
- Ferrant, P., 1998. Fully nonlinear interactions of long-crested wave packets with a three dimensional body. In: Proceedings of the 22nd International Conference on Numerical Ship Hydrodynamics, Washington, DC, pp. 403–415.
- Greco, M., 2001. A Two-Dimensional Study of Green-Water Loading. Ph.D. Thesis, Norwegian University of Science and Technology, Department of Marine Hydrodynamics, NTNU, Trondheim, Norway.
- Hăđić, I., Hennig, J., Peric, M., Xing-Kaeding, Y., 2005. Computation of flow-induced motion of floating bodies. *Applied Mathematical Modelling* 29, 1196–1210.
- Hashemi, M.R., Fatehi, R., Manzari, M.T., 2012. A modified SPH method for simulating motion of rigid bodies in Newtonian fluid flows. *International Journal of Non-Linear Mechanics* 47, 626–638.
- Hirt, C.W., Nichols, B.D., 1981. Volume of fluid (VOF) method for the dynamics of free boundaries. *Journal of Computational Physics* 39 (1), 201–225.
- Hu, C., Kashiwagi, M., 2009. Two-dimensional numerical simulation and experiment on strongly nonlinear wave–body interactions. *Journal of Marine Science and Technology* 14, 200–213.
- Kajtar, J., Monaghan, J.J., 2008. SPH simulations of swimming linked bodies. *Journal of Computational Physics* 227, 8568–8587.
- Koshizuka, S., Nobe, A., Oka, Y., 1998. Numerical analysis of breaking waves using the moving particle semi-implicit method. *International Journal of Numerical Methods in Fluids* 26, 751–769.
- Longuet-Higgins, M.S., Cokelet, C.D., 1976. The deformation of steep surface waves on water, a numerical method of computation. *Proceedings of the Royal Society of London A350*, 1–26.
- Marrone, S., Antuono, M., Colagrossi, A., Colicchio, G., Le Touzé, D., Graziani, G., 2011a. δ –SPH model for simulating violent impact flows. *Computer Methods in Applied Mechanics and Engineering* 200, 1526–1542.
- Marrone, S., Colagrossi, A., Antuono, M., Lugni, C., Tulin, M.P., 2011b. A 2D+t SPH model to study the breaking wave pattern generated by fast ships. *Journal of Fluids and Structures* 27, 1199–1215.
- Marrone, S., 2012. Enhanced SPH Modeling of Free-Surface Flows with Large Deformations. Ph.D. Thesis, University of Rome, Sapienza (Italy), Electronic version available at URL https://wiki.manchester.ac.uk/spheric/index.php/SPH_PhDs.
- Marsh, A.P., Prakash, M., Semercigil, S.E., Turan, Ö.F., 2010. A shallow-depth sloshing absorber for structural control. *Journal of Fluids and Structures* 26, 780–792.
- May, D.A., Monaghan, J.J., 2003. Can a single bubble sink a ship? *American Journal of Physics* 71 (September (9)), 842–849.
- Molteni, D., Colagrossi, A., 2009. A simple procedure to improve the pressure evaluation in hydrodynamic context using the SPH. *Computer Physics Communications* 180 (6), 861–872.
- Monaghan, J.J., Gingold, R.A., 1983. Shock simulation by the particle method SPH. *Journal of Computational Physics* 52, 374–389.
- Monaghan, J.J., Kos, A., 1999. Solitary waves on a Cretan beach. *Journal of Waterway, Port, Coastal and Ocean Engineering* 125 (3), 145–154.
- Monaghan, J.J., Kos, A., 2000. Scott Russell's wave generator. *Physics of Fluids* 12 (March (3)).
- Monaghan, J.J., Kos, A., Issa, N., 2003. Fluid motion generated by impact. *Journal of Waterway, Port, Coastal and Ocean Engineering* 129 (6), 250–259.
- Morris, J.P., Fox, P.J., Zhu, Y., 1997. Modeling low Reynolds number incompressible flows using SPH. *Journal of Computational Physics* 136, 214–226.
- Naito, S., Sueyoshi, M., 2002. A numerical study on complicated motions of floating bodies. In: Proceeding of the Sixth International Ship Stability Workshop, Webb Institute, New York.
- Oger, G., Doring, M., Alessandrini, B., Ferrant, P., 2006. Two-dimensional SPH simulations of wedge water entries. *Journal of Computational Physics* 213, 803–822.
- Omidvar, P., Stansby, P.K., Rogers, B.D., 2012. Wave body interaction in 2D using smoothed particle hydrodynamics (SPH) with variable particle mass. *International Journal for Numerical Methods in Fluids* 68, 686–705.
- Omidvar, P., Stansby, P.K., Rogers, B.D., 2013. SPH for 3D floating bodies using variable mass particle distribution. *International Journal for Numerical Methods in Fluids* 72 (4), 427–452, <http://dx.doi.org/10.1002/fld.3749>.
- Peskin, C.S., 1977. Numerical analysis of blood flow in the heart. *Journal of Computational Physics* 25, 220–252.
- Randles, P.W., Libersky, L.D., 1996. Smoothed Particle Hydrodynamics: some recent improvements and applications. *Computer Methods in Applied Mechanics and Engineering* 139, 375–408.
- Sethian, J.A., 1999. Level Set Methods and Fast Marching Methods: Evolving Interfaces in Computational Geometry, Fluid Mechanics, Computer Vision, and Materials Science. Cambridge University Press.
- Shao, S., Gotoh, H., 2004. Simulating coupled motion of progressive wave and floating curtain wall by SPH-LES model. *Coastal Engineering Journal* 46 (2), 171–202.
- Ulrich, C., Rung, T., 2012. Multi-physics SPH simulations of launching problems and floating body interaction. In: Proceeding of the 31st International Conference on Ocean, Offshore and Arctic Engineering (OMAE), June 10–15, Rio de Janeiro (2012).
- Vinje, T., Breivig, P., 1981. Nonlinear ship motions. In: Proceedings of the Third International Conference on Numerical Ship Hydrodynamics, Paris, France, pp. IV3-1–IV3-10.
- Vugts, J., 1968. The hydrodynamic coefficients for swaying, heaving and rolling cylinders in a free surface. *International Shipbuilding Progress* 15, 251–276.
- Yabe, T., Xiao, F., Utsumi, T., 2001. The constrained interpolation profile method for multiphase analysis. *Journal of Computational Physics* 169 (2), 556–593.
- Yang, J., Stern, F., 2012. A simple and efficient direct forcing immersed boundary framework for fluid–structure interactions. *Journal of Computational Physics* 231, 5029–5061.